Article

Chinese Science Bulletin

Geophysics

June 2011 Vol.56 No.16: 1691–1699
doi: 10.1007/s11434-011-4487-y

Uppermost mantle structure of the North China Craton: Constraints from interstation Pn travel time difference tomography

LI ZhiWei[1,2], HAO TianYao[1*] & XU Ya[1]

[1]*Key Laboratory of Petroleum Resources Research, Institute of Geology and Geophysics, Chinese Academy of Sciences, Beijing 100029, China;*
[2]*Key Laboratory of Dynamical Geodesy, Institute of Geodesy and Geophysics, Chinese Academy of Sciences, Wuhan 430077, China*

Received October 21, 2010; accepted March 16, 2011

The uppermost mantle is the key area for exchange of heat flux and material convection between the crust and lithospheric mantle. Spatial variations of lithospheric thinning and dynamic processes in the North China Craton could inevitably induce the velocity heterogeneity in the uppermost mantle. In this study, we used Pn arrivals from permanent seismic stations in North China and surrounding regions to construct a tomographic image of the North China Craton. The tomographic method with Pn travel time difference data were used to study the velocity variations in the uppermost mantle. Pn velocities in the uppermost mantle varied significantly in the Eastern, Central and Western blocks of the North China Craton. This suggests that the lithosphere beneath different blocks of the North China Craton have experienced distinct tectonic evolutions and dynamic processes since the Paleozoic. The current uppermost mantle has been imprinted by these tectonic and dynamic processes. Fast Pn velocities are prominent beneath the Bohai Bay Basin in the Eastern Block of the North China Craton, suggesting residuals of the Archean lithospheric mantle. Beneath the Tanlu Fault Zone and Bohai Sea, slow Pn velocities are present in the uppermost mantle, which can be attributed to significant lithospheric thinning and asthenospheric upwelling. The newly formed lithospheric mantle beneath Yanshan Mountain may be the dominant reason for the existence of slow Pn velocities in this region. Conversely, the ancient lower crust and lithospheric mantle already have been delaminated. In the Central Block, significant slow Pn velocities are present in Taihangshan Mountain, which also extends northward to the Yinchuan-Hetao Rift on the northern margin of the Ordos Block and Yinshan Orogen. This characteristic probably is a result of hot asthenospheric upwelling along the active tectonic boundary on the margin of the Western Block. The protracted thermal erosion and underplating of hot asthenospheric upwelling may induce lithospheric thinning and significant slow velocities in the uppermost mantle. Fast velocities beneath the Western Block suggest that the thick, cold and refractory Archean lithospheric keel of craton still is retained without apparent destruction.

North China Craton, Lithospheric thinning, Uppermost mantle, Pn travel time difference, Cratonic destruction

Citation: Li Z W, Hao T Y, Xu Y. Uppermost mantle structure of the North China Craton: Constraints from interstation Pn travel time difference tomography. Chinese Sci Bull, 2011, 56: 1691–1699, doi: 10.1007/s11434-011-4487-y

A craton consists of ancient continental crust and subcontinental lithospheric mantle (SCLM). Due to its relatively small density, high melting point and large thickness (~200 km), the cratonic lithosphere can be preserved on the surface of the Earth and become the most stable tectonic unit [1]. Although most Precambrian cratons have maintained their stability since their formation in the Paleoproterozoic, some of them have experienced significant destruction. For example, the Eastern Block of the North China Craton (NCC) was formed in the Early Precambrian, and has lost a significant proportion of its lithospheric keel (more than 100 km thick) since the Paleozoic. The thick lithospheric mantle has been replaced by depleted asthenosphere or oceanic mantle, and the properties of the lithospheric mantle also have been essentially modified. This indicates lithospheric modification and even destruction of the Eastern Block of the NCC (Figure 1) [1–6]. Although lithospheric thinning and modification of lithospheric properties and thermal state have been characterized by many geochemical and geophysical studies, the dynamic mechanism of cratonic

*Corresponding author (email: tyhao@mail.iggcas.ac.cn)

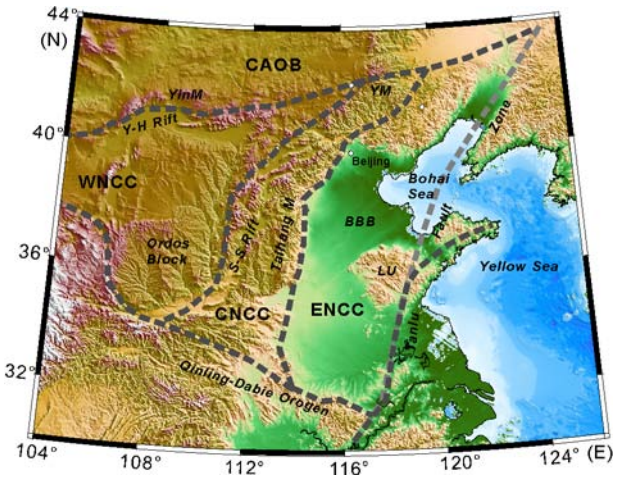

Figure 1 Simplified tectonic map of the NCC (after [4]). ENCC, Eastern Block of the NCC; CNCC, Central Block of the NCC; WNCC, Western Block of the NCC; CAOB, Central Asian Orogen Belt; LU, Luxi Uplift; YinM, Yinshan Mountain; YM, Yanshan Mountain; Y-H Rift, Yinchuan-Hetao Rift; S-S Rift, Shaanxi-Shanxi Rift; BBB, Bohai Bay Basin.

destruction still is widely disputed. Thermal-chemical erosion and delamination are two contrasting hypotheses for NCC destruction [1–3,6,7]. The delamination hypothesis states that the lower crust and upper mantle were laterally foundered into the asthenosphere due to gravity instability. The hot asthenospheric upwelling replaced the former lower crust and upper mantle [8–11]. In contrast, the thermal-chemical erosion hypothesis proposes that small amounts of SCLM were gradually digested by asthenospheric upwelling, and induced final destruction of the lithosphere [3,12]. While the delamination and thermal-chemical erosion hypotheses differ, both include alterations of thickness, physical and chemical properties, and thermal states. According to the delamination hypothesis, the ancient lower crust and lithospheric mantle sank into the asthenosphere and were replaced by the newly formed lithospheric mantle. Conversely, the thermal-chemical erosion hypothesis states that mineral composition and rheology were modified only at the lower part of lithospheric mantle, and the current preserved lithospheric mantle still remains ancient [1].

Spatial variation of lithospheric thickness shows significant discrepancy in different blocks of the NCC. Significant lithospheric thinning took place in the Eastern Block of the NCC, and the current lithospheric thickness varies from 60–100 km in this region. The Central Block of the NCC also shows lithospheric thinning to some extent. Although the entire area of the Western Block of the NCC still remains stable, thinned lithosphere also is found in some marginal areas. Seismological results from receiver function and surface wave tomography indicate that lithospheric thickness in the Ordos Block can reach 160–200 km [5,13, 14]. This suggests that the block is stable. However, a thinner lithosphere (~100 km) has been revealed in the Yinchuan-Hetao Rift on the northern margin of Ordos Block, and in the Shaanxi-Shanxi Rift and Taihangshan Mountain in the Central Block. This indicates significant lithospheric thinning and destruction. Other than the thickness variation of the lithosphere, distinct discrepancies of velocity structure also are present by the seismic travel time tomography in the crust and upper mantle [15,16]. Meanwhile, significant spatial variations of lithospheric thinning and destruction of the NCC have been revealed by the abovementioned results, and even the Central-Western blocks shows some signs of lithospheric thinning.

The uppermost mantle is the key area for exchange of heat flow and material convection between the crust and lithospheric mantle. Spatial variations of lithospheric thinning and dynamic processes in the NCC could inevitably induce velocity heterogeneity in the uppermost mantle. Thus, it is possible to investigate spatial variation and dynamic mechanisms of cratonic destruction using the velocity structure of the uppermost mantle. Pn waves dive into the mantle from the base of the crust and travel along the uppermost mantle. Temperature, pressure, composition and anisotropy vary the velocity of the uppermost mantle and affect the Pn travel time. Thus, Pn travel times provide an important avenue to study dynamic processes of continental deformation and differentiation [17–20]. Given the uneven distribution of earthquakes and stations in the NCC, relatively large earthquake mislocations may contaminate the velocity imaging by absolute travel time data from sparse seismic arrays. In this study, we used relative travel time data (e.g., interstation Pn travel time difference data) to construct a tomographic image of the uppermost mantle in the NCC. Our tomographic results provide further constraints on deep tectonics, spatial variations and dynamic mechanisms with respect to destruction of the NCC.

1 Methods and data

1.1 Tomographic methods with interstation Pn travel time difference data

Standard Pn travel time tomography utilizes the absolute Pn travel time data to inverse the velocity structure of the uppermost mantle. Event and station delays accommodate variations of crustal velocity and thickness, and earthquake mislocation [17,18,20,21]. Assuming an isotropic velocity model in the uppermost mantle, Pn travel time residuals can be approximately described by the following equation [18]:

$$\Delta t_{ij} = t_{ij}^{\mathrm{o}} - t_{ij}^{\mathrm{c}} = \Delta t_i^{\mathrm{st}} + \Delta t_j^{\mathrm{eq}} + \sum_{k=1}^{N} d_{ijk} s_k , \quad (1)$$

where Δt_{ij} is the Pn travel time residual. t_{ij}^{o} and t_{ij}^{c} are the observed and calculated Pn travel times from the *j*th earthquake to the *i*th station. Δt_i^{st} is the difference between observed and calculated travel times traveling from the Moho discontinuity to the *i*th station, which relates to crustal velocity and thickness. Δt_j^{eq} is the difference between

observed and calculated travel time from the *j*th event to the Moho discontinuity, which also relates to crustal velocity and thickness and focal depth. d_{ijk} is the ray path length in the *k*th cell, and s_k is the slowness perturbation of this cell.

Due to the difficulty of relocating earthquakes with only Pn travel time data, event and station delays are needed to minimize the bias of earthquake mislocation and heterogeneity of crustal velocity. As shown in the appendix, when one earthquake approximately lies on the great circle passing through two stations, but not between them, Pn wave travel times along the overlapped ray paths are very close (< ~0.1 s). Thus, interstation Pn travel time differences cannot easily be contaminated by earthquake mislocations and complex crustal velocity structure near the source. The velocity structure also can be largely improved after the inversion [22–24]. Moreover, the undulated Moho discontinuity model also can be introduced into the inversion to simultaneously improve the tomographic image.

For one event, the interstation Pn travel time difference recorded by station *i* and *j* can be presented as

$$\begin{aligned}\Delta t_{ij} = t_i - t_j &= \left(\sum_{k=1}^{N_i} d_{ik}s_{ik} + \Delta t_i^{\mathrm{eq}} + \Delta t_i^{\mathrm{sta}}\right) \\ &\quad - \left(\sum_{k=1}^{N_j} d_{jk}s_{jk} + \Delta t_j^{\mathrm{eq}} + \Delta t_j^{\mathrm{sta}}\right) \\ &= \left(\sum_{k=1}^{N_i} d_{ik}s_{ik} - \sum_{k=1}^{N_j} d_{jk}s_{jk}\right) \\ &\quad + (\Delta t_i^{\mathrm{eq}} - \Delta t_j^{\mathrm{eq}}) + (\Delta t_i^{\mathrm{sta}} - \Delta t_j^{\mathrm{sta}}),\end{aligned} \quad (2)$$

where t_i and t_j are the Pn travel times at station *i* and *j*. Δt_{ij} is the interstation travel time difference. d_{ik} and d_{jk} are the *k*th ray path lengths traveling through the uppermost mantle, N_i and N_j segments in total. S_{ik} and S_{jk} are the corresponding Pn wave slowness at the *k*th ray path segment. Δt_i^{eq} and Δt_j^{eq} are the travel times from the event to the Moho discontinuity. $\Delta t_i^{\mathrm{sta}}$ and $\Delta t_j^{\mathrm{sta}}$ are the travel times from the Moho discontinuity to the stations. In equation (2), the origin time of event in Δt_i^{eq} and Δt_j^{eq} has been eliminated, and only the effect of event mislocation (especially the error of focal depth) has been retained. Based on the analyses in Appendix, Δt_i^{eq} and Δt_j^{eq} in equation (2) are almost the same when the earthquake approximately lies on the great circle passing through the two stations. Hence, the interstation Pn travel time difference can be expressed as:

$$\Delta t_{ij} = t_i - t_j = (\Delta t_i^{\mathrm{sta}} - \Delta t_j^{\mathrm{sta}}) + \left(\sum_{k=1}^{N_i} d_{ik}s_{ik} - \sum_{k=1}^{N_j} d_{jk}s_{jk}\right), \quad (3)$$

where the effect of the event has been eliminated, and the event mislocation has no effect on the Pn travel time difference. Thus, this approach can be implemented in areas with sparse seismic arrays and large earthquake mislocations, such as the Western Block of the NCC and the Bohai Sea.

1.2 Data

The data used in this study were obtained from the Chinese Seismic Network and the International Seismological Centre (ISC) (1980–2008). The focal depths of selected events were shallower than 30 km, and the α angle between the back azimuths from the event to the two stations was less than 6° (Figure S2). The distance between two stations for the interstation Pn travel time difference was greater than 20 km to ensure enough sampling of the uppermost mantle. For data selection, only travel time difference data with residuals less than 4.0 s and 10% of total travel time difference were selected. Finally, a set of 9815 interstation Pn travel time differences were selected for the inversion. The events, stations and ray paths are shown in Figure 2. The data coverage is exceptionally good in most areas of the NCC, but is poor in the marginal areas of the NCC. Due to the advantage of the interstation Pn travel time difference tomographic method, events located in the Bohai Sea and Yellow Sea also could be involved in the inversion, which is usually not possible for standard Pn tomography due to its large earthquake mislocation problem.

The averaged Pn velocity (~8.0 km/s) of the uppermost mantle was determined by linear fitting with selected interstation Pn travel time difference data, and it was consistent with previous studies [18,19,21]. Figure 3(a) shows the reduced travel time *versus* epicenter distance for Pn arrivals. Figure 3(b) shows the interstation Pn wave travel time difference *versus* epicenter distance difference from one earthquake to two stations. The linear trend was clear and the slope equaled the averaged Pn velocity of the uppermost

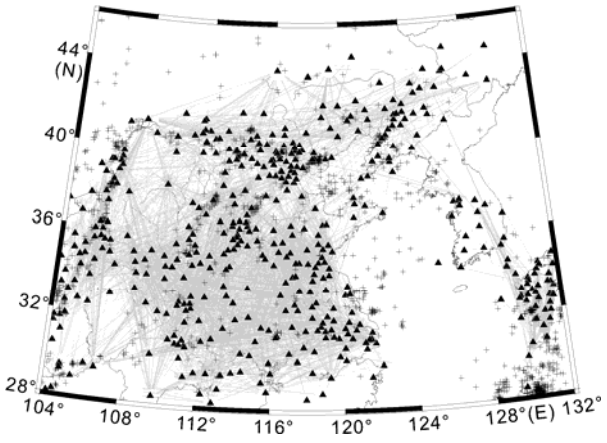

Figure 2 Map of interstation Pn travel time difference data used in this study. Black triangles indicate the seismic stations, black crosses are the earthquakes, and gray lines show the ray paths approximately sampling the uppermost mantle between two stations, which are implemented into the tomographic inversion.

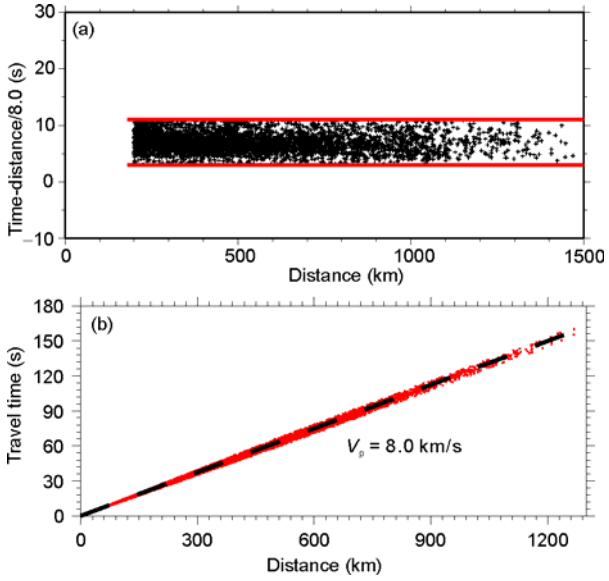

Figure 3 (a) Plots of reduced travel times *versus* epicenter distance for Pn arrivals involved in the inversion (reduced velocity is 8.0 km/s). (b) Plots of interstation Pn wave travel time differences *versus* epicenter distance difference from one earthquake to two stations (dashed line represents the synthetic travel time with an averaged velocity of 8.0 km/s in the uppermost mantle).

mantle (~8.0 km/s). Most of the back azimuth differences of interstation Pn travel time difference data were less than 3° (Figure 4), which satisfied the hypothesis of interstation Pn travel time difference tomographic method (e.g. the Pn wave travel times on the overlapped ray paths are approximately the same).

2 Results

The cell size used to solve the travel time equations was 0.5°×0.4°. Average crustal P wave velocity of 6.2 km/s and crustal thickness of 34 km were adapted in the inversion after several trials. The average Pn wave velocity of 8.0 km/s from linear fitting also was used in the inversion. The undulated Moho discontinuity model of CRUST2.0 (http://igppweb.ucsd.edu/~gabi/crust2.html) was taken into account to calculate the Pn travel time. Trials suggest that the velocity images remain closely similar even though the crustal velocity and Moho depth varied from 6.0–6.4 km/s and 32–36 km, respectively. This result verified that the interstation Pn travel time difference was not sensitive to the initial crustal model. In standard Pn tomographic method, station delay could reflect the influence of crustal velocity and thickness beneath the station. Because the undulated Moho discontinuity model of CRUST2.0 was used for Pn travel time calculations, most of station delays were less than 0.2 s, and only some of them were relatively large (~0.6 s) at Taihangshan Mountain, Shaanxi-Shanxi Rift and the marginal regions with strong crustal velocity and thickness variations (Figure S6). Thus, it is difficult to analyze the trend of crustal thickness with station delays [18]. After the inversion, residuals of interstation Pn wave travel time differences clearly were minimized with all back azimuths (Figure 5) and lengths of Pn ray paths traveling in the uppermost mantle (Figure 6). A posteriori residual standard deviation was 0.54 s, a 57% reduction from that of the starting model, which suggests that the preferred model can fit the observed data very well.

We performed the checkerboard test to estimate resolution of our tomographic result. Figure 7 shows the recovered images with 1.5°×1.2° and 2°×1.6° grid spacing models with a perturbation of 3%. Results indicate that for much of the NCC the velocity anomalies were well resolved. In the northern part of the NCC and sea areas, the resolution was relatively low because of sparse ray path coverage. Our tomographic results were largely consistent with previous tomographic results in much of the NCC [15,18,19,21,

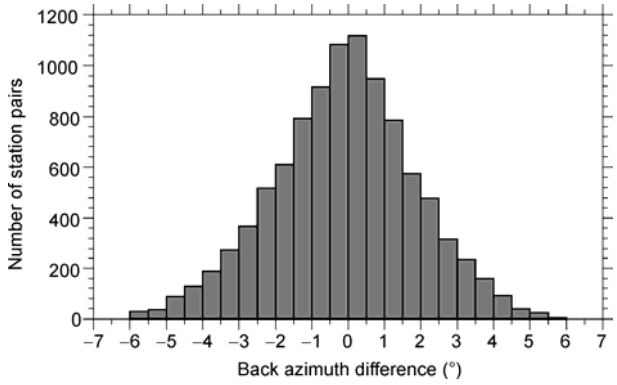

Figure 4 Distribution of back azimuth differences of interstation Pn travel time difference data.

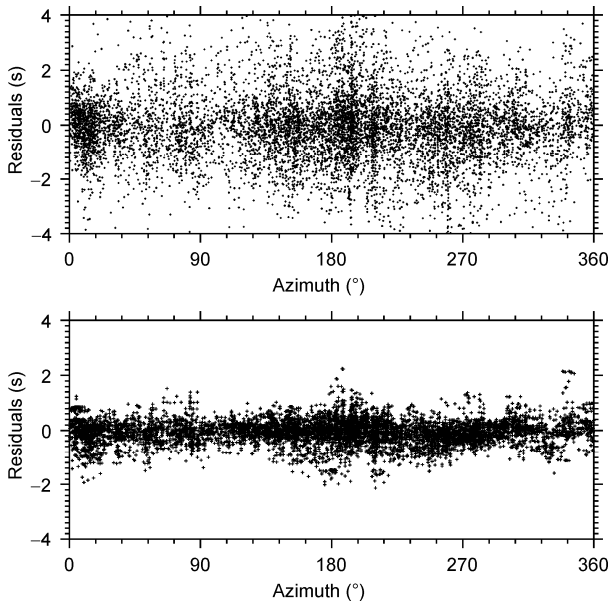

Figure 5 Plots of residuals of interstation Pn wave travel time differences *versus* back azimuths of ray path before (upper) and after (below) the tomographic inversion.

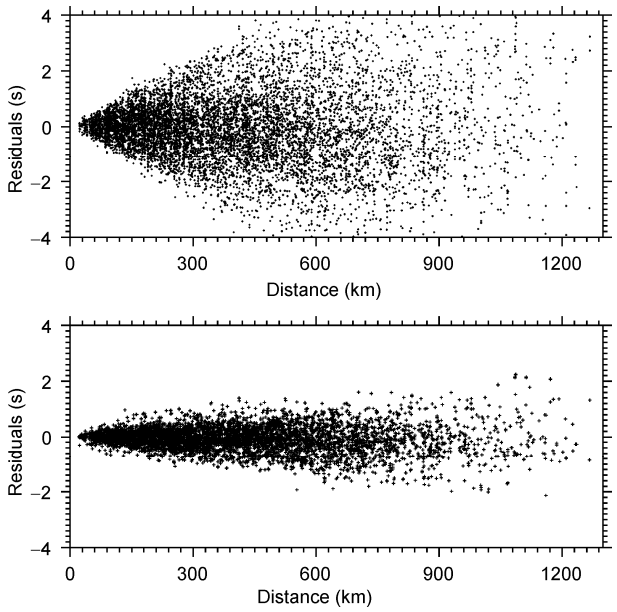

Figure 6 Plots of residuals of interstation Pn wave travel time difference *versus* the lengths of Pn wave ray paths traveling in the uppermost mantle before (upper) and after (lower) the tomographic inversion.

25–27], but more details of the uppermost mantle are shown in our results, which could provide further information to analyze spatial variations of destruction of the NCC.

Figure 8 shows a Pn velocity image of the uppermost mantle in the NCC and surrounding regions. In the Eastern Block, fast velocities of the uppermost mantle (~8.2 km/s) in the Bohai Bay Basin were pronounced. Conversely, the Luxi Uplift and its southern areas (the Tanlu Fault Zone, the Jiaodong peninsula and the Yanshan Mountain) all were characterized by slow velocities (7.8–7.9 km/s). In the Central Block, slow velocities (~7.8 km/s) were a dominant feature in the Shaanxi-Shanxi Rift and Taihangshan Mountain. The slow velocities also extended northward to the Yinchuan-Hetao Rift and Yinshan Mountain to the north of the Western Block. In contrast, fast velocities reached 8.1 km/s in the southern part of the Central Block, which differed greatly from slow velocities in the Qinling-Dabie Orogen. In the Western Block of the NCC, significant fast velocities were present in much of the Ordos Block.

3 Interpretation and discussion

Previous results of petrology and lithospheric thickness provide evidences for spatial variations of lithospheric thinning, which imply different mechanisms of cratonic destruction in different areas of the NCC. Our tomographic images of the uppermost mantle also clearly indicate that significant discrepancies exist in the NCC. The velocity structure near the crust-mantle boundary may provide another important clue to investigate cratonic destruction and its dynamic processes in the NCC.

3.1 Eastern Block of the NCC

Significant fast velocities were found beneath the Bohai Bay Basin. Similar characteristics also have been found in previous tomographic results of the lithospheric mantle [15, 18,19,21,27–29]. Local tomographic images from P and PmP travel time data also indicate obvious fast velocities at 42 km depth [30]. Since 42 km is already deep in the uppermost mantle in North China, the tomographic images at this depth represent the velocity structure of the uppermost mantle, which is consistent with our results from Pn travel time difference data. Moreover, fast S wave velocity struc-

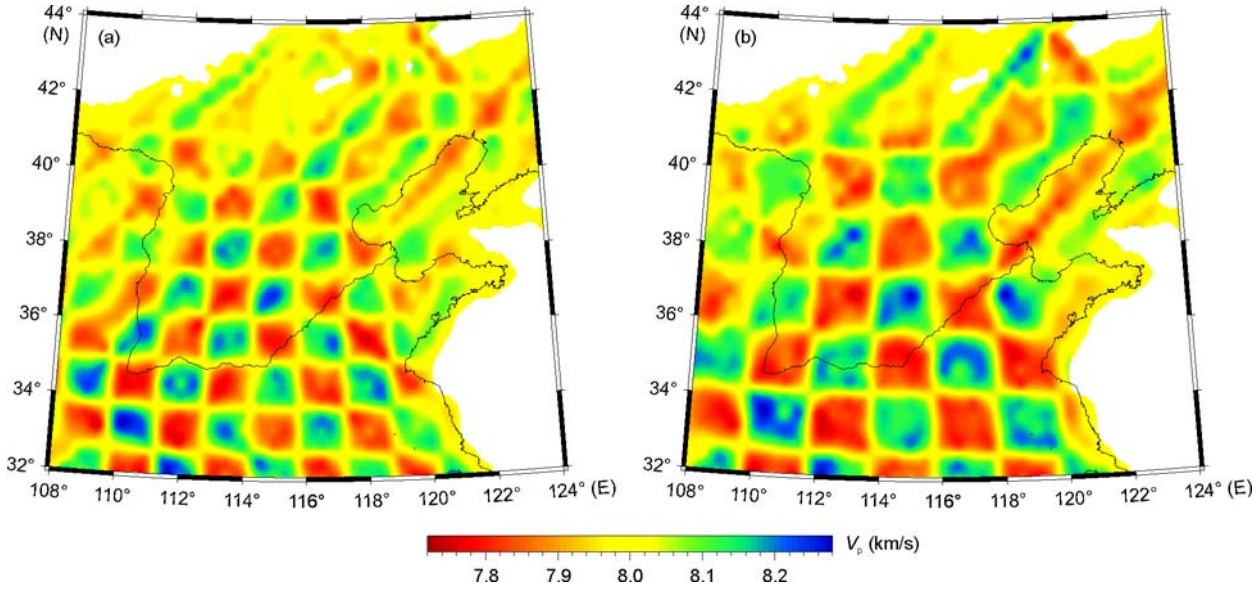

Figure 7 Checkerboard resolution tests with different anomaly sizes. (a) 1.5°×1.2°; (b) 2°×1.6°.

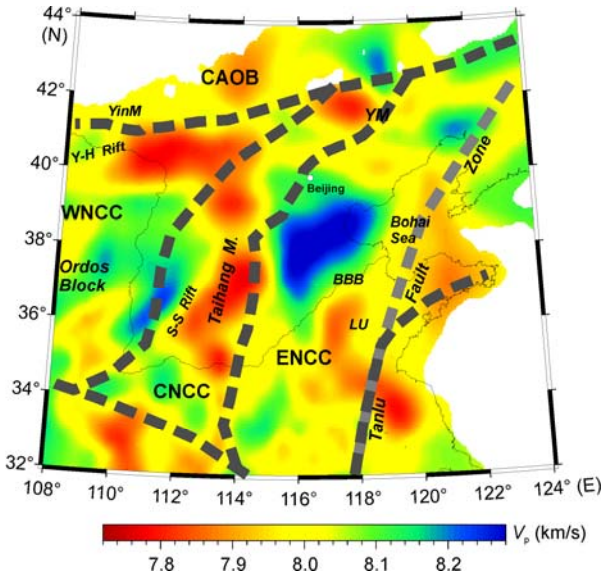

Figure 8 Pn wave velocities of the uppermost mantle in the NCC.

tures also have been found in the surface wave tomography beneath Bohai Bay Basin [14]. Receiver function migrations depict the lithospheric thickness of the Eastern Block, and indicate that the thinnest lithosphere (60–80 km) was located in the Bohai Sea, the Luxi Uplift and the Tanlu Fault Zone [5]. In contrast, in the Bohai Bay Basin, the lithosphere was to 80–110 km in thickness. Huang et al. [14] inferred that the lower crust and lithospheric mantle to as deep as 130 km in the North China Basin already have been modified. However, from surface wave tomography, some residuals of fast velocities still remain in the uppermost mantle beneath Bohai Bay Basin, which agrees with our results. Hence, we infer that the fast velocity anomaly in the uppermost mantle suggests residuals of Archean lithospheric mantle.

As the region with the thinnest lithospheric mantle (60–70 km), the Tanlu Fault Zone has slow velocity layers in the crust [5,7,31–33]. Previous studies show that the Tanlu Fault Zone has cut through the crust and reaches to the lithospheric mantle. Hence, it may have become the corridor of asthenospheric upwelling during a period of continental extension of the eastern Block and lithospheric thinning in the Mesozoic and Cenozoic [31]. This also may be the reason for the thickened crust-mantle transition zone and significant low velocity anomaly in the uppermost mantle beneath the Tanlu Fault Zone. Cratonic destruction in this area may be largely attributed to protracted thermal erosion and underplating [7,12,32]. This also suggests that the lithospheric weak zone plays an important role in cratonic destruction of the NCC.

The Luxi Uplift has significantly slow velocities in the uppermost mantle. According to previous studies, the crustal and lithospheric thicknesses vary from 32–36 km and 60–70 km, respectively [32]. Gao et al. [10] found evidence for lithospheric delamination in Feixian of the Luxi Uplift, and inferred that the dominant mechanism of cratonic destruction in the Luxi Uplift is lithospheric delamination. If this inference is correct, the significantly slow velocities in the uppermost mantle could be attributed to effects of high temperatures due to hot asthenospheric upwelling after lithospheric thinning.

Yanshan Mountain is also characterized by apparent slow velocities in the uppermost mantle. Delamination was supported as the dominant mechanism of cratonic destruction in this area [9,34], and may have induced the SCLM sinking into the asthenosphere. Thus, the newly formed and thinned lithosphere after delamination of ancient lithosphere could be the primary reason for slow velocities in the uppermost mantle at Yanshan Mountain.

3.2 Central Block of the NCC

As part of the Daxinganling-Taihangshan-Wuyishan gravity lineament, crustal and lithospheric thicknesses intensively vary beneath the eastern and western sides of the Central Block of the NCC. The gravity lineament also becomes the suture zone, which separates Eastern and Western blocks [1, 35]. The uppermost mantle beneath the Central Block is dominated by significantly slow velocities. The slow velocities were closer to eastern Taihangshan Mountain and extended to the northern margin of the Ordos Block, which is largely consistent with the distribution of late Mesozoic and Cenozoic basalts and the Shaanxi-Shanxi and Yinchuan-Hetao rifts [1,36]. We infer that the slow velocities here may be attributed to magmatic activity in the upper mantle.

In previous travel time tomography studies, slow velocity zones to 500 km depth, and extending in a N-S trend, also have been found at the base of lithospheric mantle in the Central Block [15,27]. The characteristics of slow velocity were clearer in the S waves rather than P waves [27]. Since S wave velocities are more sensitive to variation of temperature compared with P wave velocities [37], the slow velocity anomaly could be primarily induced by high temperature. Zhao et al. [27] indicated that the Central Block may have behaved as a sublithospheric corridor for hot mantle material, which may have induced reactivation of the Archean NCC. If this inference is correct, the significantly slow velocities beneath Taihangshan Mountain and the Yinchuan-Hetao Rift in our tomographic image suggest that the influence of the asthenosphere upwelling has already reached the uppermost mantle and crust-mantle boundary. Our results also provide possible evidence that the dominant cause of lithospheric destruction may be protracted thermal erosion and underplating. Zheng et al. [34] found thickened crust and a thick crust-mantle transition zone at Taihangshan Mountain by receiver functions, and inferred that the leading cause of lithospheric destruction also could be protracted thermal erosion and underplating, which is similar with the Tanlu Fault Zone. In addition, results from receiver function and surface wave tomography studies both indicate that the lithosphere has been thinned to 100 km in the

Yichuan-Hetao and Shaanxi-Shanxi rifts [13,14], and suggest that lithospheric thinning occurred in these areas.

3.3 Western Block of the NCC

Due to sparse seismic stations and earthquakes in the Western Block of the NCC, sparse ray path coverage reduces the resolution in this area. Thus, the block boundaries were not clearly delineated in our tomographic image. However, tectonic features at a regional scale generally were reflected in the velocity image of the uppermost mantle. Obvious fast velocities are found in most areas of the Western Block, which is consistent with previous Pn tomography at larger scales [18,19]. Seismic travel time tomography also indicated that the fast velocity anomaly beneath the Western Block extends to 200 km depth or deeper [15,16,27,28]. Given the thick lithosphere (160–200 km) [13,14], relatively low heat flow (~40 mW/m^2) [38], absence of volcanoes or strong earthquake activity, we infer that the lithosphere of the Ordos Block remains a stable Archean craton. Conversely, marginal areas of the Ordos Block become weak zones for lithospheric thinning. Based on results from receiver function and surface wave tomography studies [13, 14], the lithosphere has been thinned to 100 km in the Central Block to the east of the Ordos Block, and strong thinning to 80 km has occurred in the Yinchuan-Hetao Rift and Yinshan Mountain to the north of the Ordos Block. As the suture of the Yangtze and the North China blocks, the lithosphere in the Qinling-Dabie Orogen also was thinned to 100–130 km to the south of the Ordos Block. In our tomographic results, the above mentioned areas for lithospheric thinning all showed significant slow velocities, suggesting considerable influence from lithospheric thinning to the uppermost mantle. Based on the locations of slow velocities, we infer that the asthenospheric upwelling may have been obstructed by the ancient and stable lithosphere of the Ordos Block. As a result, upwelling acted on a pre-existing weak zone on the margin of the Ordos Block and formed the upwelling corridor of hot sublithospheric materials. The upwelling corridor also exacerbated lithospheric destruction and thinning. The Western Block may not have been obviously affected by Phanerozoic lithosphere destruction entirely, and the cratonic keel of the Western Block apparently remains stable. However, if the lithospheric thickness of 160 km in the Western Block indeed has been thinned to some extent, as shown in the surface wave tomography [14], then the mechanism for lithospheric destruction here should be protracted thermal erosion and underplating, which was also the case in the Central Block.

3.4 Spatial variation of cratonic destruction and the discrepancy of dynamic processes

Cratonic destruction and lithospheric thinning not only altered lithosphere thickness, but also affected the petrology and thermal state of the lithosphere [1]. The spatial variations of lithospheric structure also were clearly indicated by our uppermost Pn velocity image, and may have been associated with different destruction mechanisms and dynamic processes in different areas. Clear discrepancies of lithospheric destruction exist in the Eastern, Central and Western blocks of the NCC. The lithosphere of the Eastern Block is in destruction mode and is thinned overall, while the Western Block basically remains stable. As for the Central Block, the lithospheric thickness increases from east to west, suggesting cratonic destruction is exacerbated in this direction [7]. This also is consistent with subduction and dehydration of the stagnant slab of the Pacific Plate, which could result in the increase of melting and fluid in the mantle, and induce upwelling of hot mantle materials [7,39–41]. As the stagnant slab of the Pacific Plate only reached Taihangshan Mountain to the west [28], it is reasonable that the entire lithospheric destruction and thinning only took place to the east of Taihangshan Mountain. In addition, subduction of the Pacific Plate promoted the mantle convection and upwelling of hot mantle in the Central and Western blocks [7], which thinned the weak lithosphere on the margin of the Ordos Block, and also decreased the velocity in the uppermost mantle. Benefiting from the obstruction of the thick Archean lithosphere in the Ordos Block, the Western Block has not been destroyed in any obvious manner. However, if the destruction had happened to a certain extent in the Western Block, we infer that the protracted thermal erosion and underplating should be the dominant mechanism.

4 Conclusions

The uppermost mantle structure of the NCC was constructed by using interstation Pn travel time difference data. Pn velocities in the uppermost mantle vary significantly in different blocks, suggesting the lithosphere of the NCC has experienced distinct tectonic evolution and dynamic processes since the Paleozoic. The current uppermost mantle has been imprinted by these tectonic and dynamic processes. The fast velocity anomaly in the uppermost mantle of the Bohai Bay Basin suggests residuals of the Archean lithospheric mantle. The slow velocities beneath the Tanlu Fault Zone and Bohai Sea area can be largely attributed to intensive lithospheric thinning and hot asthenospheric upwelling. The newly formed and thinned lithosphere after delamination could be the reason for the slow velocity in the uppermost mantle at Yanshan Mountain. The protracted thermal erosion and underplating are likely responsible for lithospheric thinning and slow velocities in the uppermost mantle in the Central Block. The lithosphere of the Western Block remains relatively stable and shows characteristics of the Archean craton, which is consistent with the fast velocities in the uppermost mantle.

We are grateful to the Academician Liu G D for the direction. We also thank Dr. Li J and Dr. Zhao L F for their constructive comments and helpful modifications of the manuscript. We thank two anonymous reviewers for their insightful reviews and thoughtful comments, which improved the manuscript. This work was supported by the National Natural Science Foundation of China (90814011), Open Fund of Key Laboratory of Geodetection (China University of Geosciences, Beijing), Ministry of Education (GDL0905), Fund of China Geological Survey (GZH200900504) and the China Postdoctoral Science Foundation (20090460511).

1 Wu F Y, Xu Y G, Gao S, et al. Lithospheric thinning and destruction of the North China Craton (in Chinese). Acta Petrol Sin, 2008, 24: 1145–1174
2 Fan W M, Menzies M A. Destruction of aged lower lithosphere and accretion of asthenosphere mantle beneath eastern China. Geotecton Metallogen, 1992, 16: 171–180
3 Menzies M A, Fan W, Zhang M. Palaeozoic and Cenozoic lithoprobes and the loss of > 120 km of Archaean lithosphere, Sino- Korean Craton, China. In: Prichard H M, Alabaster T, Harris N B W, et al., eds. Magmatic Processes and Plate Tectonics. Geol Soc Spec Pub, 1993, 76: 71–78
4 Zhao G, Wilde A, Cawood A, et al. Archean blocks and their boundaries in the North China Craton: Lithological, geochemical, structural and P-T path constraints and tectonic evolution. Precambrian Res, 2001, 107: 45–73
5 Chen L, Wang T, Zhao L, et al. Distinct lateral variation of lithospheric thickness in the Northeastern North China Craton. Earth Planet Sci Lett, 2008, 267: 56–68
6 Zheng Y F, Wu F Y. Growth and reworking of cratonic lithosphere. Chinese Sci Bull, 2009, 54: 3347–3353
7 Zhu R X, Zheng T Y. Destruction geodynamics of the North China Craton and its Paleoproterozoic plate tectonics. Chinese Sci Bull, 2009, 54: 3354–3366
8 Gao S, Rudnick R, Carlson R W, et al. Re-Os evidence for replacement of ancient mantle lithosphere beneath the North China Craton. Earth Planet Sci Lett, 2002, 198: 307–322
9 Gao S, Rudnick R, Yuan H, et al. Recycling lower continental crust in the North China Craton. Nature, 2004, 432: 892–897
10 Gao S, Rundnick R, Xu W, et al. Recycling deep cratonic lithosphere and generation of intraplate magmatism in the North China Craton. Earth Planet Sci Lett, 2008, 270: 41–53
11 Gao S, Zhang J F, Xu W L, et al. Delamination and destruction of the North China Craton. Chinese Sci Bull, 2009, 54: 3367–3378
12 Xu Y G. Thermo-tectonic destruction of the Archean lithospheric keel beneath the Sino-Korean Craton in China: Evidence, timing and mechanism. Phys Chem Earth, 2001, 26: 747–757
13 Chen L, Cheng C, Wei Z. Seismic evidence for significant lateral variations in lithospheric thickness beneath the central and western North China Craton. Earth Planet Sci Lett, 2009, 286: 171–183
14 Huang Z X, Li H Y, Zheng Y J, et al. The lithosphere of North China Craton from surface wave tomography. Earth Planet Sci Lett, 2009, 288: 164–173
15 Tian Y, Zhao D, Sun R, et al. Seismic imaging of the crust and upper mantle beneath the North China Craton. Phys Earth Planet Inter, 2009, 172: 169–182
16 Xu P F, Zhao D. upper-mantle velocity structure beneath the North China Craton: Implications for lithospheric thinning. Geophys J Int, 2009, 170: 1095–1099
17 Hearn T M. Anisotropic Pn tomography in the western United States. J Geophys Res, 1996, 101: 8403–8414
18 Hearn T M, Wang S, Ni J F, et al. Uppermost mantle velocities beneath China and surrounding regions. J Geophys Res, 2004, 109: B11301
19 Pei S, Zhao J, Sun Y, et al. Upper mantle seismic velocities and anisotropy in China determined through Pn and Sn tomography. J Geophys Res, 2007, 112: B05312
20 Li Z W, Roecker S, Li Z H, et al. Tomographic image of the crust and upper mantle beneath the western Tien Shan from the MANAS broadband deployment: Possible evidence for lithospheric delamination. Tectonophysics, 2009, 477: 49–57
21 Wang S Y, Xu Z H, Pei S P. Velocity structure of uppermost mantle beneath North China from Pn tomography and geological structure (in Chinese). Sci China Ser D-Earth Sci, 2003, 33(Suppl): 91–98
22 Li J. Research of seismic tomography in Capital Circle Area from Pn and PmP wave travel time inversions (in Chinese). Dissertation for the Doctoral Degree. Beijing: Institute of Geophysics, Chinese Administration of Earthquake, 2003. 1–110
23 Phillips W S, Rowe C A, Steck L K. The use of interstation P wave arrival time differences to account fore regional path variability. Geophys Res Lett, 2005, 32: L11301
24 Seward A M, Henderson C M, Smith E G C. Models of the upper mantle beneath the central North Island, New Zealand, from speeds and anisotropy of subhorizontal P waves (Pn). J Geophys Res, 2009, 114: B01301
25 Liang C, Song X, Huang J. Tomographic inversion of Pn travel times in China. J Geophys Res, 2004, 109: B11304
26 Li C, van der Hilst R, Nafi T M. Constraining P-wave velocity variations in the upper mantle beneath Southeast Asia. Phys Earth Planet Inter, 2006, 154: 180–195
27 Zhao L, Allen R M, Zheng T, et al. Reactivation of an Archean craton: Constraints from P- and S-wave tomography in North China. Geophys Res Lett, 2009, 36: L17306
28 Huang J, Zhao D. High-resolution mantle tomography of China and surrounding regions. J Geophys Res, 2006, 111: B09305
29 Li Z W, Xu Y, Hao T Y, et al. Seismic tomography and velocity structure in the crust and upper mantle around Bohai Sea area (in Chinese). Chinese J Geophys, 2006, 49: 797–804
30 Lei J, Xie F, Lan C, et al. Seismic images under the Beijing region inferred from P and PmP data. Phys Earth Planet Inter, 2008, 168: 134–146
31 Chen L, Zheng T, Xu W. A thinned lithospheric image of the Tanlu Fault Zone, northeastern China, constructed from wave equation based receiver function migration. J Geophys Res, 2006, 111: B09312
32 Zheng T, Zhao L, Zhu R. Insight into the geodynamics of cratonic reactivation from seismic analysis of the crust-mantle boundary. Geophys Res Lett, 2008, 35: L08303
33 Xu Y G, Li H Y, Pang C J, et al. On the timing and duration of the destruction of the North China Craton. Chinese Sci Bull, 2009, 54: 3379–3396
34 Zheng T, Zhao L, Xu W W, et al. Insight into modification of North China Craton from seismological study in the Shandong Province. Geophys Res Lett, 2008, 35: L22305
35 Hao T Y, Liu Y K, Duang C. The characteristic of geophysical field in the east China and adjacent regions and its tectonics significance (in Chinese). Chin J Geophys, 1997, 40: 677–690
36 Tang Y, Zhang H, Ying J. Asthenosphere-lithospheric mantle interaction in an extensional regime: implication from the geochemistry of Cenozoic basalts from Taihang mountains, North China Craton. Chem Geol, 2006, 233: 309–327
37 Cammarano F, Goes S, Vacher P, et al. Inferring upper-mantle temperatures from seismic velocities. Phys Earth Planet Inter, 2003, 138: 197–222
38 Hu S B, He L J, Wang J Y. Heat flow in the continental area of China: A new data set. Earth Planet Sci Lett, 2000, 179: 407–419
39 Zhao D. Global tomographic images of mantle plumes and subducting slabs: Insight into deep Earth dynamics. Phys Earth Planet Inter, 2004, 146: 3–34
40 Lei J, Zhao D. P-wave tomography and origin of the Changbai intraplate volcano in northeast Asia. Tectonophysics, 2005, 397: 281–295
41 Lei J, Zhao D. Global P-wave tomography: On the effect of various mantle and core phases. Phys Earth Planet Inter, 2006, 154: 44–69

Supporting Information

Appendix

Figure S1 Standard deviations of interstation first P arrival differences to 200 times changes in source location for different interstation distances.

Figure S2 Observation system sketch of interstation travel time differences from one earthquake to two stations.

Figure S3 Sketch of Pn wave traveling from an earthquake to the uppermost mantle.

Figure S4 Plots of inter-ray path distance with the same epicenter distances (e.g., the length of *BD* in Figure S2) *versus* interstation distance.

Figure S5 Sketch of Pn wave traveling from the uppermost mantle to the seismic station.

Figure S6 Pn wave velocities of the uppermost mantle with station delays (crosses) in the NCC.

The supporting information is available online at csb.scichina.com and www.springerlink.com. The supporting materials are published as submitted, without typesetting or editing. The responsibility for scientific accuracy and content remains entirely with the authors.

Appendix

Figure S1 shows the influences of earthquake mislocation to the interstation travel time difference. The crustal velocity was 6.2 km/s and the mantle velocity was the same as the iasp91 model. The travel time was calculated by using the finite difference method [20]. Initial positions of events were located on the grid of 0.25°×0.25° with a depth of 25 km. 200 times perturbations for sources were implemented in three dimensions with 20 km Gaussian random noise to simulate the earthquake mislocation (the origin time of event was eliminated from equation [3]). When the earthquake was located on the same side and near the great circle passing through the two stations, the nearest distance to the two stations was greater than ~200 km (the distance that Pn became the first arrival). In addition, earthquake mislocation had little effects on travel time difference between two stations (RMS was less than 0.13 s). Thus, when the loca-

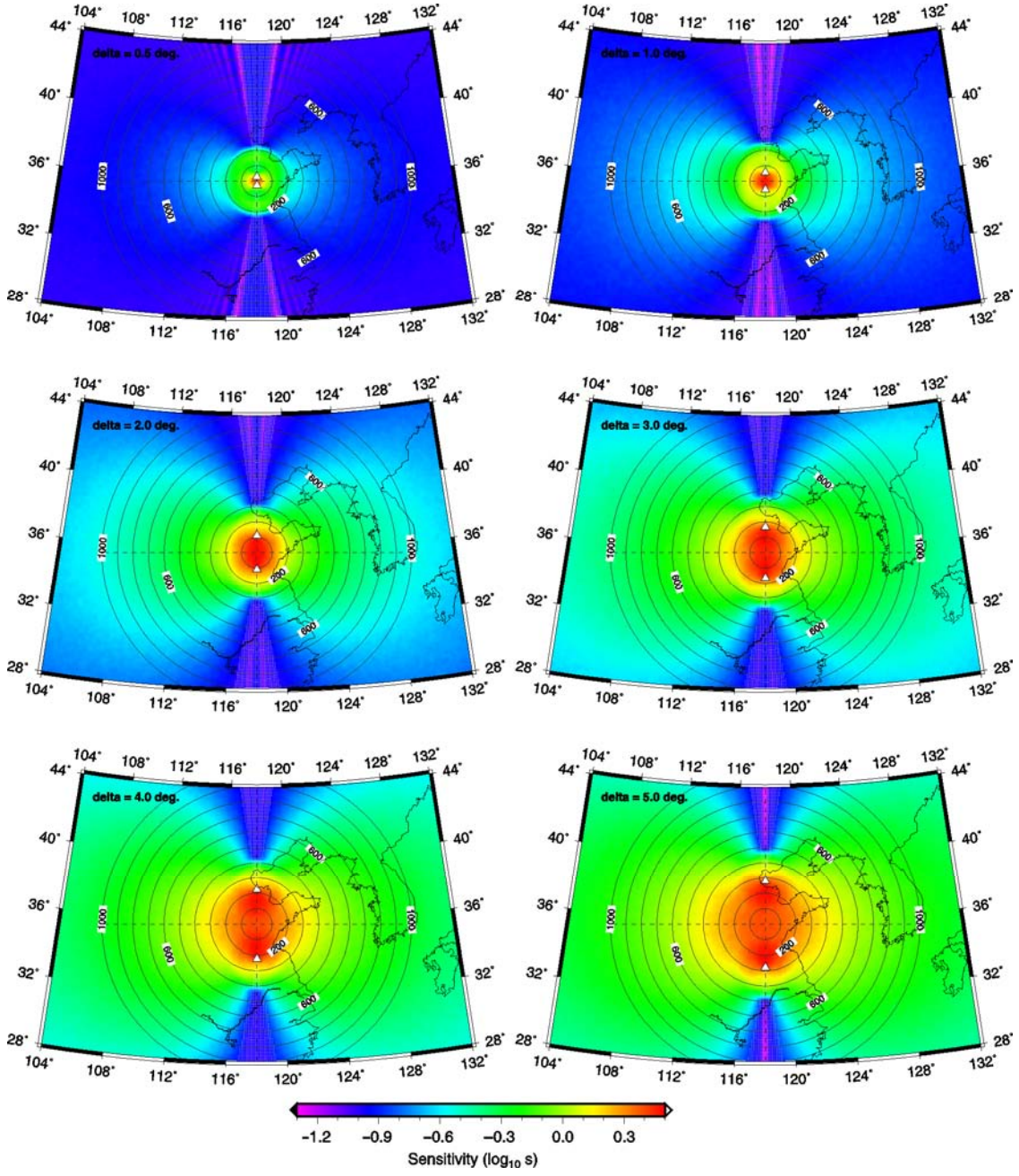

Figure S1 Standard deviations of interstation first P arrival differences to 200 times changes in source location for different interstation distances. Concentric circles are plotted in increments of 100 km from the middle of two stations. Note that the shaded area indicates the region within 10° azimuth of the straight line through two stations. In this area, standard deviations of P wave arrival-time differences were less than ~0.1 s (~$\log_{10}$-0.9 s) (after [23]).

tions of one earthquake and two stations satisfy some criterion (α less than ~6° in Figure S2), the interstation Pn travel time difference was not sensitive to earthquake mislocation. As shown in Figure S3, the ray paths (*OA* and *OB* in Figure S3) travel in the crust with the same velocity, $(\Delta t_i^{\mathrm{eq}} - \Delta t_j^{\mathrm{eq}})$ and in equation (2) should be zero. For the actual crustal structure, the velocity and Moho depth differences along the two ray paths induce $(\Delta t_i^{\mathrm{eq}} - \Delta t_j^{\mathrm{eq}})$ to not be equal to zero.

If α in Figure S2 was less than 6°, the two ray paths of *OA* and *OB* nearly overlapped. In the 1-D model, following Snell's Law, we know $\sin(\theta) = \mathrm{V}_1 / \mathrm{V}_2$, the distance between piercing points (*A* and *B* in Figure S3) on the Moho discontinuity can be represented as:

$$d_{AB} = 2h \frac{\mathrm{V}_1}{\sqrt{\mathrm{V}_2^2 - \mathrm{V}_1^2}} \sin(\alpha). \quad \text{(S1)}$$

For a typical crustal model (V_1=6.2 km/s, V_2=8.0 km/s with α = 6°), $d_{AB} \approx 0.26h$, which is the upper limit value of d_{AB}. d_{AB} will decrease when α becomes smaller. When the earthquake was located on the 0 km and crustal thickness was 35 km, d_{AB} reached 9 km. For regional tomographic studies with scales of tens of kilometers or more, the velocity structure varied gently. Hence, travel times from one earthquake to two stations were approximately the same. α also could be decreased to minimize the error to an acceptable level, especially when the velocity structure varied significantly near the earthquake.

Because the earthquake and the two stations were located near the great circle, part of the ray paths traveling through the uppermost mantle approximately overlapped (*CB* and *CD* in Figure S2). We analyzed the relationships among the inter-ray path distances (e.g. *BD* in Figure S2), the interstation distance and α (Figure S4). The length of *BD* increased with increase of epicenter distance and interstation distance. If α becomes smaller, the length of *BD* also becomes smaller. For example, when the interstation distance was 800 km and epicenter distance was 200 km, the length of *BD* was less than 18 km. This suggests that the ray paths from the earthquake to the nearest station approximately overlapped. The overlapped ray paths had almost the same travel time for the regional velocity model. Hence, interstation Pn travel time difference is mainly attributed to the velocity structure of the uppermost mantle between the two stations.

The distance between two stations can reach several hundreds of kilometers. Thus, crustal velocity and thickness may strongly vary, and the station elevation also may differ as much as several kilometers (Figure S5). Thus, the travel time difference from the Moho discontinuity to two stations of $(\Delta t_i^{\mathrm{sta}} - \Delta t_j^{\mathrm{sta}})$ was not always zero and needed to be preserved in equation (3). In our tomographic method, we introduced the undulated Moho discontinuity model to the 1-D initial model and made the calculation more accurate. Station delays also used in the inversion to minimize the influence of the heterogeneous crust beneath the two stations.

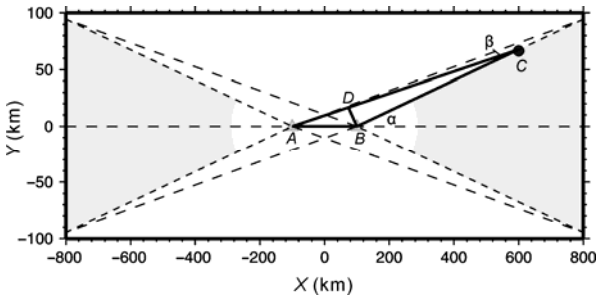

Figure S2 Observation system sketch of interstation travel time differences from one earthquake to two stations. Gray triangles (*A* and *B*) indicate the two seismic stations. Black circles (*C*) are positions of earthquakes. The lines of *CA* and *CB* represent the ray path from earthquake *C* to the stations *A* and *B* in the uppermost mantle, respectively, and *AB* is the interstation distance. Gray shadows indicate the area where the earthquake nearly locates in the great circle passing through the two stations with maximum angle of α, and the Pn wave becomes the first arrival. β is the angle between the ray paths from the earthquake to the two stations, which is always less than α. *D* is the point at the ray path *CA*, which makes *CD* equals *CB*. Hence, *BD* represents the maximum distance between the ray paths *CA* and *CB* with the same epicenter distances to the earthquake. The ray path difference (*AD*) is used in the tomographic inversion.

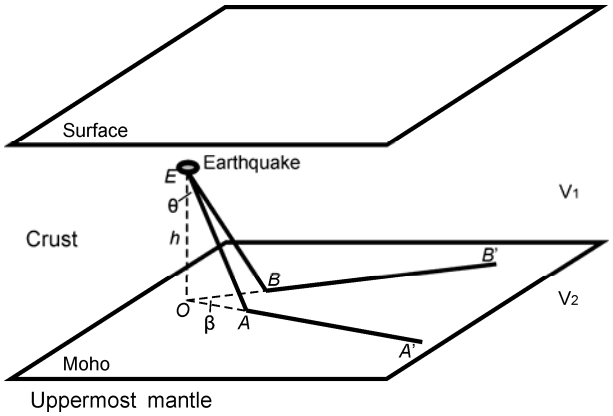

Figure S3 Sketch of Pn wave traveling from an earthquake to the uppermost mantle. V1 represents the averaged crustal velocity, and V2 represents the averaged velocity of the uppermost mantle. *O* is the projection of an earthquake on the Moho discontinuity, while *A* and *B* are the incidence points of ray paths on the Moho discontinuity. *h* represents the perpendicular distance from the earthquake to the Moho discontinuities. θ is the incidence angle of ray path. *AA'* and *BB'* represent the Pn ray paths to the two stations.

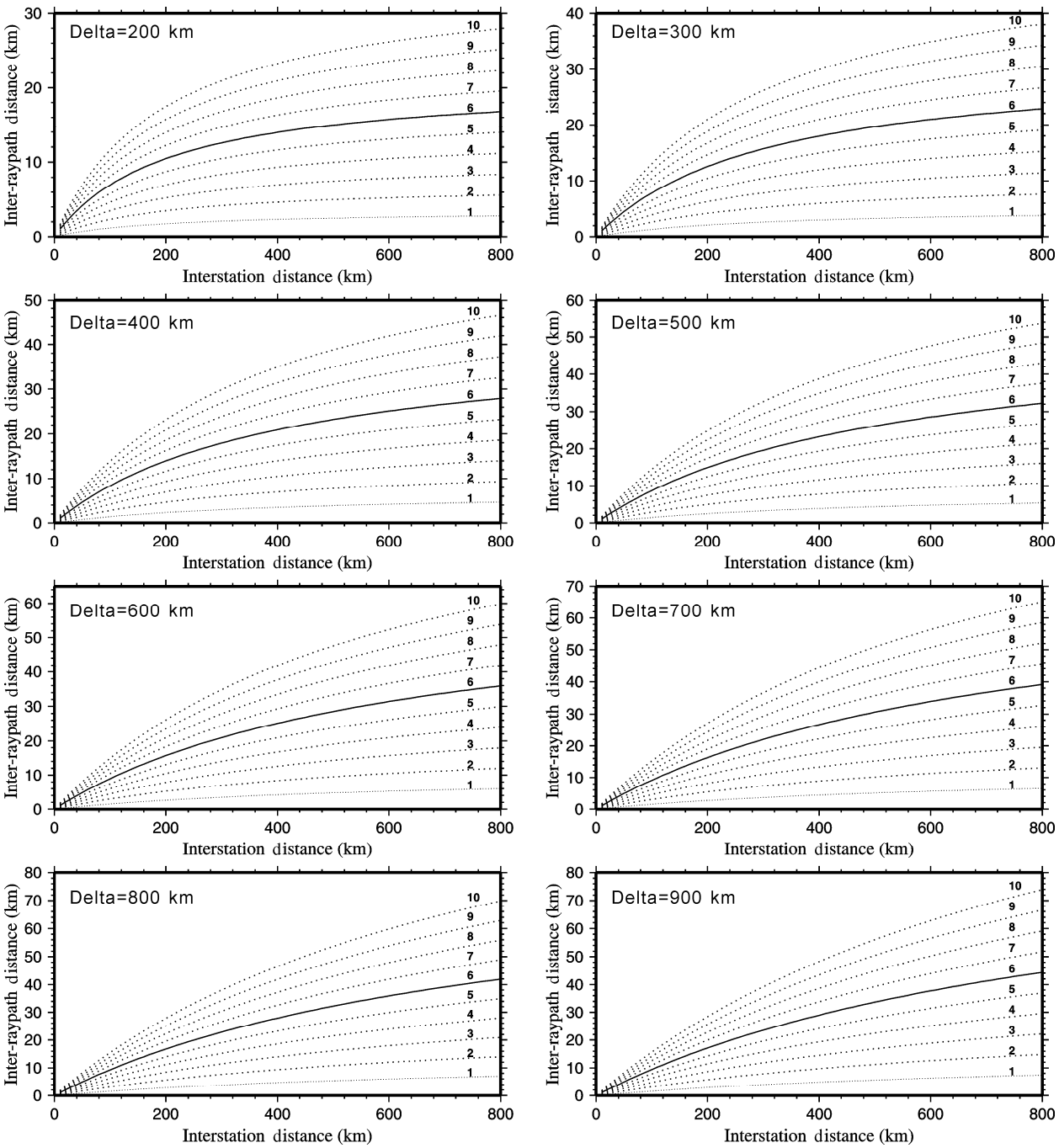

Figure S4 Plots of inter-ray path distance with the same epicenter distances (e.g., the length of *BD* in Figure S2) *versus* interstation distance. The closed epicenter distance is shown in the upper-left corner of each map, and the azimuth α (e.g. the angle α in the Figure S2) is shown on the line in each map. Solid lines in each map indicate inter-ray path distance with $\alpha=6°$.

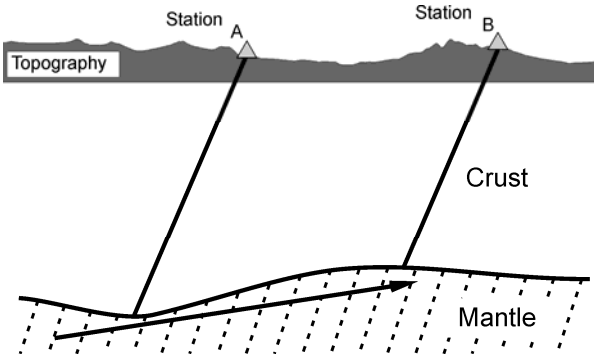

Figure S5 Sketch of Pn wave traveling from the uppermost mantle to the seismic station. The Pn wave travel time can be affected by the undulation of the Moho discontinuity, and then the station delay is needed in the tomographic inversion.

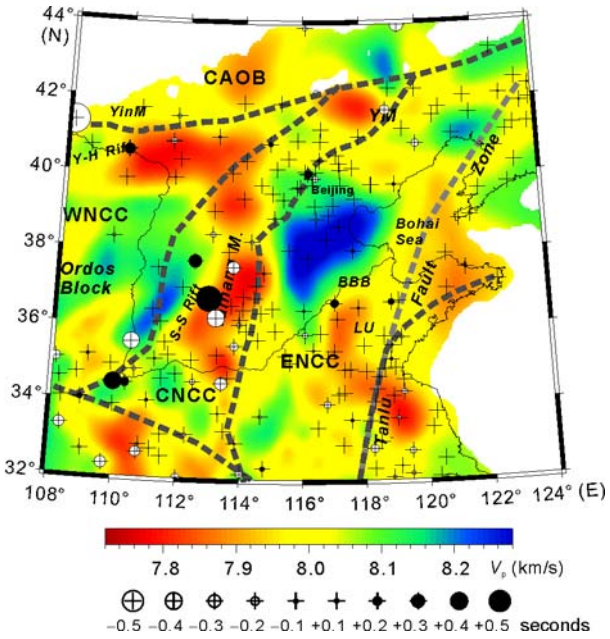

Figure S6 Pn wave velocities of the uppermost mantle with station delays (crosses) in the NCC.